

Uncertainty analysis of depth predictions from seismic reflection data using Bayesian statistics

Dimitrios G. Michelioudakis^{1*}, Richard W. Hobbs¹, and Camila C.S. Caiado²

¹*Department of Earth Sciences, University of Durham, Durham, U.K.*

²*Department of Mathematical Sciences, University of Durham, Durham, U.K.*

Key Points

- Uncertainty in velocity models
- Pre-stack deghost filters
- Gaussian process emulation
- Bayesian History matching
- Probabilistic imaging

Summary

Estimating the depths of target horizons from seismic reflection data is an important task in exploration geophysics. To constrain these depths we need a reliable and accurate velocity model. Here, we build an optimum 2D seismic reflection data processing flow focused on pre – stack deghosting filters and velocity model building and apply Bayesian methods, including Gaussian process emulation and Bayesian History Matching (BHM), to estimate the uncertainties of the depths of key horizons near the borehole DSDP-258 located in the Mentelle Basin, south west of Australia, and compare the results with the drilled core from that well. Following this strategy, the tie between the modelled and observed depths from DSDP-258 core was in accordance with the $\pm 2\sigma$ posterior credibility intervals and predictions for depths to key horizons were made for the two new drill sites, adjacent the existing borehole of the area. The probabilistic analysis allowed us to generate multiple realizations of pre-stack depth migrated images, these can be directly used to better constrain interpretation and identify potential risk at drill sites. The method will be applied to constrain the drilling targets for the upcoming International Ocean Discovery Program (IODP), leg 369.

* Correspondence to: dimitrios.michelioudakis@durham.ac.uk

1. Introduction

Velocity model building is a critical step in seismic reflection processing. An optimum velocity field can generate flat common image gathers (CIGs) and well focused images in time or depth domain. Nevertheless, taking into account the noisy and band limited nature of the seismic reflection data and the ambiguity in the velocity estimation, the generated velocity field is only our best estimate of a set of possible velocity fields [Bickel, 1990; Tieman, 1994; Kosloff & Sudman, 2002]. Hence, all the calculated depths and the images produced are just our best approximation of the true subsurface.

Although incorporating anisotropic parameters [Thomsen, 1986; Alkhalifah & Tsvankin, 1995; Alkhalifah, 1997] during the velocity analysis stage can assist to constrain better the depth results [Hawkins *et al.*, 2001], the non - uniqueness of the velocity field still remains an open problem as different velocity fields can lead to nearly equally flat arrivals in CIG [Chitu *et al.*, 2008]. The problem is worse in the absence of any well log information, where the velocity field cannot be calibrated, rendering the final structural image only a sample among the most probable images, as an optimally focused image doesn't necessarily mean accuracy of depths [Al-Chalabi, 1994, 2014].

Conventionally, the initial estimation of the reflection time and root mean square velocities (V_{rms}) for each geological layer is based on picking the local maxima on a semblance spectrum [Neidell & Taner, 1971], computed from common - mid point (CMP) gathers. The ambiguity associated with the velocity model building is shown schematically in figure 1. The CMP gather is Normal Moveout (NMO) corrected with 3 slightly different velocity fields after 4.2 s TWT, but visually the reflection arrivals appear equally flat (Fig. 1a, 1b). Earlier than 4.2 s, the maxima are less ambiguous to pick and the degree of precision of each picked value is higher. However, the velocity model building for deeper structures is compromised by the low depth to offset ratio and the attenuated frequency and amplitude content of the signal. This velocity - depth issue, limits the sensitivity of residual moveout to velocity changes and indicates that the semblance spectrum as a tool lacks the resolution to provide us with a unique velocity model [Lines, 1993]. Tomographic inversion in the migrated domain for velocity estimation is inherently non - unique [Jones, 2014] as it is trying to match the observed time values by choosing different combinations of depth (z) and slowness (s) values [Jones, 2010]. Multiple realizations of the same boundary can be created, all having slightly different pairs of z , s (Fig. 1c).

Attempts have been made to incorporate statistical information in seismic reflection data processing

55 and perform uncertainty analysis for constraining velocities or depth results [*Abrahamsen et al.*, 1991;
56 *Landa*, 1991; *Chitu et al.*, 2008; *Lewis et al.*, 2015; *Messud et al.*, 2017]. The uncertain nature of the
57 produced velocity field can be addressed by statistically analysing the given velocity model to quantify the
58 uncertainty associated with each pick. In this paper, we will use high resolution 2D seismic reflection data
59 and develop a robust processing flow to effectively combine seismic analysis with Bayesian methods such as
60 Gaussian Process emulation and Bayesian History Matching (BHM), to quantify uncertainties in velocity
61 models using a suite of algorithms called BRAINS (from Bayesian Regression Analysis In Seismology
62 [*Caiado et al.*, 2012]). This paper can be considered as an extension of [*Caiado et al.*, 2012], where a part
63 of the methodology was initially outlined. However, this is the first time that the model with the statistical
64 techniques are formalised and detailed. Also, to our knowledge, this is the first time that a combination of
65 Gaussian Process emulators and Bayesian History Matching is implemented as part of a seismic processing
66 flow.

67 The objective of this study is to estimate the uncertainties associated with the depths of drilling
68 targets for the upcoming International Ocean Discovery Program (IODP) project, leg 369, located in
69 Mentelle Basin, SW Australia (Fig. 2a) [*Borissova*, 2002; *Direen et al.*, 2007]. In this area, stratigraphic
70 information is available from the Deep Sea Drilling Project (DSDP) borehole 258, which penetrated a series
71 of carbonate oozes, limestones, black shales and sands [*Davies et al.*, 1974] (fig. 2b), deposited during the
72 Cretaceous Hothouse period (90-70 Ma). Part of the sedimentary sequence may contain evidence for sudden
73 decrease in atmospheric CO₂ concentrations with associated periods of glaciation [*Kuypers et al.*, 1999].
74 By drilling and recovering samples from targeted geological sequences, we can collect valuable information
75 about the paleotemperature regime, biotic records, ocean circulation and tectonic history of the region.

76 Poor core recovery and the lack of wireline sonic information from DSDP-258, means that the depth
77 predictions of key horizons is based entirely on the velocity values inferred from surface seismic data. As
78 the sensitivity of differential move out, during the velocity analysis stage using a semblance spectrum, is
79 linked to the frequency content of the wavelet in pre - stack data (CMP gathers) [*Chen and Schuster*,
80 1999; *Jones*, 2010], we opt to follow a complete seismic reflection processing flow with the main focus on
81 improving the temporal resolution of the seismic data. This is achieved by eliminating the source and
82 receiver ghost notches in the pre - stack domain using inverse deghosting filters. The latter approach
83 allows us to perform pre - stack depth migration (preSDM) on the ghost free CMP gathers, and produce
84 an image with optimum spatial resolution and focusing, which aids to better constrain the interpretation.

85 We use the probabilistically derived velocity estimates to retrieve the depth information for key bound-

86 aries, tied to borehole 258 and make predictions for the depths of drilling targets for the two planned wells
87 4B–4C, located adjacent to the borehole DSDP 258. Finally, as the probabilistic approach produces a pos-
88 terior distribution of velocity values, we generate a set of velocity fields and produce different realizations
89 of pre - stack depth migration (preSDM) images for the line segment intersecting the planned wells (Fig.
90 2a, 2b).

91 **2. Geological setting of the study area**

92 The western and southern margins of Australia are defined as the two arms of a triple junction that formed
93 during the final stages of the Gondwana breakup [*Powell et al.*, 1988; *Royer & Coffin*, 1992; *Direen et al.*,
94 2007].

95 One of the most important geological features of that region is the Mentelle Basin (MB). It is a sparsely
96 explored, deep water sedimentary basin, located between the Naturaliste Plateau and the southern part of
97 the Western Australian Shelf. Seismic images based on early seismic surveys showed that Mentelle basin is
98 elliptical in shape, with minor and major axes 200 km east-west and 220 km north-south, respectively. Its
99 main depocenter, is believed to contain sediments from Cretaceous to Holocene which produce an interval
100 of more than 3.0 s two-way-time (TWT) on the seismic image [*Borissova*, 2002; *Bradshaw et al.*, 2003].
101 These sediments are possibly underlain by older sediments from an earlier rifting event. The presence of
102 a thick sedimentary sequence in the MB gives a petroleum potential similar to that of the southern Perth
103 Basin [*Borissova*, 2002].

104 The stratigraphic features of the MB are not delineated as this area is sparsely drilled. Nevertheless, the
105 results of the borehole site (DSDP 258) in conjunction with newly processed and reprocessed seismic data
106 from GA S280 and S310 surveys, Shell Petrel Development Survey and Geoscience Australia Continental
107 Margins Surveys 18 [*Sargent et al.*, 2011], allowed the division of the stratigraphy of MB into seismically
108 derived tectonostratigraphic megasequences [*Maloney et al.*, 2011].

109 **3. Methods**

110 **3.1 Gaussian Process emulators for modelling seismic velocities**

111 In the Bayesian framework, the expert’s knowledge about the parameters that govern a system are repre-
112 sented using prior distributions, then the available data, in conjunction with a sampling model (likelihood
113 function), are used to update our knowledge about these parameters (posterior distribution). In seismic

114 reflection processing, we can use the observed amplitudes of reflection events in a CMP gather $\{A_{ij}\}$,
 115 offsets $\{X_j\}$, recorded travel times $\{T_{ij}^{(r)}\}$ and picked $\{V_{rms_i} - T_{0_i}\}$ or derived $\{V_{int_i} - T_{0_i}\}$ pairs as prior
 116 information and we aim to quantify the uncertainty of $\{\Delta T_{0_i}, \Delta V_{rms_i}, V_{int_i}, \Delta Z_i\}$ for the horizons of inter-
 117 est. BRAINS suite [Caiado *et al.*, 2012] uses a combination of Bayesian methods, such as emulation and
 118 Bayesian History Matching, to quantify these uncertainties.

119 Our approach is based on a discrete subsurface model (Appendix A.1), with a finite number i of geo-
 120 physical layers and a given array of source (S_j) – receiver (R_j) pairs, $j = 1, \dots, m$. These are symmetrically
 121 placed around a CMP, with X_j being the distance between S_j and R_j . For every X_j and hyperbolic event
 122 (layer) i , we have observed amplitude values A_{ij} and recorded time T_{ij} . Also, for each layer we can assign
 123 a zero–offset two–way travel time T_{0_i} , its time increment ΔT_{0_i} , a root-mean-square velocity V_{rms_i} with its
 124 velocity increment ΔV_{rms_i} , an interval velocity V_{int_i} and a thickness ΔZ_i . Our model seeks to estimate
 125 variables $\{\Delta T_{0_i}, \Delta V_{rms_i}, V_{int_i}, \Delta Z_i\}$ and their relevant uncertainties, from observed data $\{A_{ij}, X_j, T_{ij}^{(r)}\}$,
 126 taking into account the prior information from picked $\{V_{rms_i}, T_{0_i}\}$ or $\{V_{int_i}, T_{0_i}\}$ pairs derived during the
 127 velocity analysis stage.

128 In the case of isotropic conditions, the recorded travel time of a wave to propagate, under the ray
 129 assumption, from seismic source S_j to detector R_j , $T_{ij}^{(r)}$, can be expressed as:

$$T_{ij}^{(r)} = \sqrt{T_{0_i}^2 + \left(\frac{X_j}{V_{rms_i}}\right)^2} + \epsilon_{ij} + e_{ij} \quad (1)$$

130 where ϵ_{ij} accounts for the model discrepancy due to propagating approximations and isotropic assumptions,
 131 e_{ij} corresponds to recording errors. Although recording error (e_{ij}), is present in a construction of a
 132 statistical model, as the observations are indirect and recorded with a finite accuracy, it is the model
 133 discrepancy term (ϵ_{ij}) that has a key role in our statistical representation. Model discrepancy integrates
 134 all the simplifications of physical laws, used to describe the model, with our incomplete knowledge about
 135 the system explored and represents our inability to build a model which depicts reality [Craig *et al.*,
 136 1997]. Thus, by including the ϵ_{ij} term not only we address the potential issue of overfitting the model to
 137 the observed data [Andrianakis *et al.*, 2015] but we also produce uncertainty estimations for the output
 138 variables of interest. As expressed in equation (1), ϵ_{ij} term represents effects related with anisotropic wave
 139 propagation (ϵ, δ anisotropic parameters) and ray tracing approximation.

140 Typically, these error terms are ignored which results in the Dix equation [Dix, 1955], where we can
 141 relate V_{rms_i} and V_{int_i} as:

$$V_{int_i} = \sqrt{\frac{T_{0_i} V_{rms_i}^2 - T_{0_{i-1}} V_{rms_{i-1}}^2}{T_{0_i} - T_{0_{i-1}}}} \quad (2)$$

142 and calculate the thickness ΔZ_i of each layer as :

$$\Delta Z_i = \frac{V_{int_i} \Delta T_{0_i}}{2} \quad (3)$$

143 Equations (2), (3) are based on the hyperbolic approximation of the recorded travel time. Including the
 144 error terms in eq. 1 allows a more robust approach, which is not restricted to hyperbolic assumptions but
 145 can express more complex models for incorporating recorded travel time from seismic rays which follow a
 146 nonnormal trajectory. We use the above equations to construct a Gaussian Process (GP) model. A GP can
 147 be thought as the generalization of the univariate Gaussian probability distribution and formally is defined
 148 as “a collection of random variables with any finite number of which having a joint Gaussian distribution”
 149 [Rasmussen & Williams, 2006]. They are well established models, applied in a variety of spatial and
 150 temporal problems [Ripley, 1991] including geostatistics [Matheron, 1973; Journel & Huijbregts, 1978] and
 151 Kalman filters [Ko & Fox, 2009]. A GP is fully defined by its mean, $m(a)$ and covariance $k(a, a')$ functions
 152 with a, a' representing samples from the random vector.

153 In this paper we will use the Gaussian Process emulators. An emulator is defined as a stochastic belief
 154 specification, which expresses probabilistic judgements for a deterministic function $f(a)$ [Craig *et al.*, 1997;
 155 O’Hagan, 2006; Vernon *et al.*, 2010; Caiado & Goldstein, 2015]. Commonly, they are expressed in the
 156 following form:

$$f_h(a) = \sum \beta_{hj} g_{hj}(a) + u_h(a) \quad (4)$$

157 where a is input value, β_{hj} unknown scalars, $g_{hj}(a)$, known deterministic functions and $u_h(a)$ is a stochastic
 158 process, normally a GP with zero mean and a square exponential covariance function. Index h represents
 159 the output variable. As a result, in equation (4) we can incorporate our beliefs and the uncertainties about
 160 each variable of the system explored.

161 In our statistical analysis, we use two emulators for uncertainty quantification. Firstly, a local (1D)
 162 emulator (Appendix A.1), where we make the assumption that a set of travel times related to a given
 163 horizon in a single CMP can be approximated as a sample of a continuous function with a hyperbolic
 164 trend. If any finite set of travel times from this hyperbolic curve is believed to follow a multivariate
 165 Gaussian distribution, we can assume that the recorded travel time curve is a GP with respect to offset x

$$\mathcal{T}_i^{(r)}(x) | \Delta T_{0(1, \dots, i)}, \Delta V_{rms(1, \dots, i)} \sim \mathcal{GP}(m_{t_i}(x), k_i(x, x')) \quad (5)$$

166 or expressed in a form consistent to equation 1 as:

$$\mathcal{T}_i^{(r)}(x) = (t_{0_i}^2 + x^2 v_{rms_i}^{-2})^{1/2} + u_i(x) \quad (6)$$

167 The first term of the right hand side represents the mean function $m_{t_i}(x)$ and the second term a stationary
 168 stochastic process with zero mean and a square exponential covariance functions $k_{t_i}(x, x')$, with the mean
 169 and covariance functions given below:

$$\begin{aligned} m_{t_i}(x) &= (t_{0_i}^2 + x^2 v_{rms_i}^{-2})^{1/2} \\ k_{t_i}(x, x') &= \sigma_{n_i} + \sigma_{s_i} \exp\left(-\frac{(x - x')^2}{d_i}\right) \end{aligned} \quad (7)$$

170 The terms x and x' define two random points from the offset space within a single CMP. Comparing
 171 equation (1) with expression (7) we can see that the hyperbolic trend of travel time equation is stored
 172 under the mean function $m_{t_i}(x)$ and the error terms ϵ_{ij} , e_{ij} are stored under the noise parameters σ_{n_i} , σ_{s_i}
 173 of the covariance function. The parameter d_i represents the length – scale of the function and defines how
 174 far the x, x' values should be to become uncorrelated. The covariance function, can be adjusted to specific
 175 applications by correctly tuning its hyperparameters (σ_{n_i} , σ_{s_i} , d_i). As our prior knowledge about their
 176 appropriate values reflects our knowledge about the system, they can be treated as constants that need to
 177 be set manually or derived from an optimization process using the training data [*Rasmussen & Williams*,
 178 2006]. In our case, the training data can be thought of as the set of prior $T_{0_i} - V_{rms_i}$, $T_{0_i} - V_{int_i}$ pairs
 179 picked during the velocity analysis stage. Based on the velocity analysis interval (spacing between two
 180 consecutive picked pairs), the picked values and also their variability along the picked velocity layer, we
 181 can manually calibrate accordingly, the noise, scale and length parameters of the covariance function and
 182 provide starting points for their values. Subsequently, the parameters are refined using a gradient search
 183 to find a local maximum in the likelihood and retrieve values in an area of high probability. Equations
 184 (5)–(7) can be formulated analogously for linking $\mathcal{T}_i^{(r)}$ with V_{int_i} and ΔZ_i , rendering the Bayesian model
 185 multidimensional.

186 Secondly, a 2D emulator expands the 1D uncertainty estimation into a 2D multi–gather representation
 187 by assuming that the variables ΔT_{0_i} , ΔV_{rms_i} , V_{int_i} and ΔZ_i , for every geophysical boundary, follow a
 188 GP over the CMP positions (x_c) along a profile (Appendix A.2). The latter, is used to constrain the

189 inter-gather areas and produce estimates in regions where we don't have available prior pick pairs.

190 3.2 Bayesian History Matching for model space reduction

191 In order to perform model calibration and reduce the parameter input space we use the approach known as
 192 Bayesian History Matching [Craig *et al.*, 1997; Vernon *et al.*, 2010]. Bayesian History Matching (BHM) is
 193 an established method and combined with emulation techniques has been tested successfully in a variety of
 194 different scientific disciplines such as reservoir modelling [Craig *et al.*, 1997; Cumming & Goldstein, 2009]
 195 climate modelling [Caiado & Goldstein, 2015] and galaxy formation modelling [Vernon *et al.*, 2010]. BHM
 196 should not be confused with the term History Matching widely used in the oil industry, as in the latter
 197 case, we are trying to match empirical data, such as production rates and observed pressure from well
 198 logs, with a complex model (normally called simulator) that is assumed to represent part of the subsurface
 199 (reservoir), where the parameters that govern the model don't include any uncertainty estimation. On
 200 the contrary through the process of BHM, all the possible models that can match our observed data
 201 are identified [Vernon *et al.*, 2010]. Following the same notation as in equation (4), in BHM, we aim to
 202 identify and iteratively discard input values, a , of the parameter space for which the evaluation of a function
 203 (emulator) $f_h(a)$ isn't likely to provide a good match to the observed data L . The parts of parameter space
 204 that are discarded are called implausible and the process of reducing the space is accomplished using the
 205 probabilistic criterion of implausibility $I_h(a)$ [Craig *et al.*, 1997; Vernon *et al.*, 2010]. The general definition
 206 of Implausibility is given below.

207 **Definition 1.** Implausibility

208 For a given choice of input value a with modelled output $f_h(a)$, observation vector L_h and taking into
 209 account all the variances present in the system $Var_h(system)$, implausibility $I_h(a)$ is defined as:

$$I_h^2(a) = \frac{\left(L_h - f_h(a)\right)^2}{Var_h(system)} \quad (8)$$

210 Large values of $I_h(a)$ indicate that, taking into account all the uncertainties of the system (denominator
 211 of Eq. 8), it is very unlikely to obtain acceptable matches between the model outputs and the observed data
 212 at input a . However, small values of $I_h(a)$ don't necessarily mean that the input value a is correct [Vernon
 213 *et al.*, 2010]. The Implausibility measure $I_h(a)$, as expressed in equation 8, refers to multidimensional
 214 models (h number of output variables). A one dimensional example of the above form, taking into account
 215 all the types of uncertainties present in our system (Eq. 1) and based on the GP model as expressed in

216 equation (5), can be formulated as:

$$I_i^2(a) = \frac{\left(L_i - E^*(T_i^{(r)}(a))\right)^2}{Var^*(T_i^{(r)}(a)) + Var(\epsilon_i) + Var(e_i)} \quad (9)$$

217 where L_i our observed data, $E^*(T_i^{(r)}(a))$, $Var^*(T_i^{(r)}(a))$ the posterior mean and posterior variance of
 218 Gaussian Process emulator and $Var(\epsilon_i)$, $Var(e_i)$ are the variances of the modelling and observation error,
 219 respectively. Index i , represent each velocity layer. The observed data L_i , for every discrete velocity layer
 220 associated with a hyperbolic event in a CMP gather, is the local maximum value of the semblance spectrum
 221 of that hyperbolic trend calculated from the observed offset X_j , amplitude values A_j and recorded time
 222 T_j . The non - implausible space is gradually reduced by applying multiple iterations of BHM. In order
 223 to identify the region of implausible input values, we use a cut - off limit based on Pukelsheim's 3σ rule
 224 (any continuous unimodal distribution at least 95% of the probability is within three sigma of the mean)
 225 [Pukelsheim, 1994]. Based on that rule, input values a for which $I_h(a) > 3\sigma$ are considered implausible and
 226 are discarded. The iterative BHM procedure is usually repeated until the difference between the regions,
 227 after successive iterations, becomes small or the posterior variance is suitably small [Andrianakis et al.,
 228 2015].

229 As BRAINS model is multidimensional ($T_i^{(r)}$ is linked with ΔT_{0_i} , ΔV_{rms_i} , $V_{int.i}$ and ΔZ_i , referred as
 230 index h in Eq. 8), we opt to built separate implausibilities for every output h . A simple combination
 231 between the implausibility measures can be performed by taking the maximum implausibility $I_M(a) =$
 232 $max I_h(a)$ which can be used to find regions of input values a with large $I_M(a)$ values. Note that the
 233 application of BHM is a fast process as it excludes the implausible space without considering the full input
 234 and output space simultaneously, dissimilar to other calibration methods such as Markov Chain Monte
 235 Carlo (MCMC) or maximum likelihood methods where the calibration is performed taking into account
 236 all input / output parameters [Andrianakis et al., 2015].

237 A pictorial example of GP emulation with BHM calibration in seismic reflection data processing is
 238 presented in figure 3. The conventional semblance spectrum plots (Fig. 3a), for a number of CMP's
 239 along a profile, are picked to derive an initial estimate of $T_0 - V_{rms}$ pairs (red circles) associated with
 240 a number of seismic boundaries (fig. 3b). The pairs don't include any sort of uncertainty measurement
 241 and are linearly interpolated between non - adjacent CMP positions (gray dashed lines). As a result, this
 242 process leads to unique $T_0 - V_{rms}$ and $Z - V_{int.}$ volumes and unique subsurface images in time and depth
 243 domain. For the statistical approach, the $T_0 - V_{rms}$ pairs along with CMP gathers which contain the

244 observed parameters $L = [A_j, X_j, T_j]$ transformed in the semblance space, are used as input data to the
 245 local (1D) GP emulator to derive an estimate of the most probable functions evaluated at each picked
 246 pair. By means of calibration, we reduce the parameter space substituting the semblance spectrum by an
 247 implausibility spectrum which is calculated using equation (8). In fig. 3c, a $Z - V_{int.}$ map is presented,
 248 with the picked pairs being spatially linked with the preSDM image shown in fig. 3d. The coloured band
 249 inside the trend indicates different levels of implausibility. In the regions where the posterior mean is far
 250 from the observed values the implausibility is considered large (red color), indicating that an input pair in
 251 that band is unlikely to give an output that will match the observations L . On the contrary, if we choose
 252 to make our pick in the lower implausibility regions (green areas), the posterior variance will decrease,
 253 with a simultaneous decrease of the non - implausible region. A further decrease of parameter space can
 254 be achieved by iteratively performing BHM in the non-implausible regions.

255 The process continues in all CMP locations where we provided prior pick information and terminates
 256 when one of the aforementioned criteria is reached. The posterior mean and variance estimations for the
 257 picked pairs, serve as a guide to perform uncertainty analysis along the profile using the multi - gather 2D
 258 emulator aiming to produce probabilistic estimates in the intra - CMP gathers area.

259 Note that the implausibility map is not restricted to the $Z - V_{int.}$ space but it is calculated for any
 260 combination of T_0 or Z with V_{rms} or $V_{int.}$ pairs. Each implausibility pair has different shape and size,
 261 locally (in every CMP location) and also laterally (along CMP locations), incorporating the different level
 262 of uncertainty in each picked pairs and spatial positions. Also, the regions between the prior information
 263 picks in each map are bounded by the posterior $\pm 2\sigma$ curves (blue dashed curves), with the posterior
 264 mean function curve (solid black curve) intersecting regions of lowest implausibility. This inter - layer
 265 representation of uncertainty can be achieved by interpolating the posterior results.

266 The final output of this process is a set of uncertainty quantification for all T_0 , V_{rms} , V_{int} and Z
 267 parameters for each horizon of interest (fig. 3d). An important by-product of the technique is that by
 268 quantifying the uncertainty of $V_{int.}$ values, we can generate a set of velocity fields bounded by the $\pm 2\sigma$
 269 curves and produce different realizations of preSDM images. The latter tool can be critical in regions with
 270 complex geology or for data rich in low frequency content and noise level, where a sole realization of imaged
 271 structures may not adequately identify risk at proposal drill sites.

272 3.3 Data preconditioning for input to BRAINS

273 As our primary goal is to develop a horizon based velocity model discretized in a number of layers (Appendix
 274 A.1), the final version of the velocity field aims to produce flat CIG gathers and focused images in time
 275 and depth domain. Therefore, the processing steps are tailored appropriately to build an optimum velocity
 276 field which will be used as prior information to BRAINS algorithm. Concurrently, in order to clarify the
 277 target horizons of the profile we shaped the amplitude spectrum by eliminating the source bubble pulse
 278 coda and the source and receiver ghost notches in the shot domain.

279 The pre-stack de-signature and deghosting process combined with the reposition of the data through
 280 the application of preSTM / preSDM, are the two key steps in the processing flow described below and
 281 they have a dual effect in improving BRAINS estimation. Firstly, by improving the temporal resolution
 282 pre - stack, sharper reflections events become apparent in CMP domain, which are transformed into well
 283 defined local maxima in the semblance space. As BRAINS and the process of BHM use the semblance
 284 spectrum (L observed data) as a tool to constrain the posterior results, the pre - stack deghosting gives
 285 extra precision to the model's outputs. Secondly, the pre - stack reposition of the data is mandatory, as
 286 it focuses the reflection events and eliminates the dip-dependence of stacking velocity ($V_{st.}$), providing a
 287 better constrain to prior information (T_0 , Z with V_{rms} , $V_{int.}$ pairs).

288 3.3.1 Time domain processing

289 The raw shot gathers for line S310-07 are provided by Geoscience Australia (detailed acquisition parameters
 290 in Table 1, processing sequence in Table 2). Initially, geometry acquisition information is imported to the
 291 profile and gun and receivers static corrections are applied to the shot gathers to compensate for the tow
 292 depths of the source and streamer. A time - invariant low cut filter is used to reduce the low frequency
 293 swell noise. The first step for the spectrum shaping is to create a debubble operator to eliminate the
 294 source's bubble pulse coda. The inverse operator is modelled using the Nucleus source modelling package
 295 [Petroleum Geo services (PGS)] which takes into account the acquisition parameters, the volume and type
 296 of air - guns and the physical parameters of the water (sound speed and temperature) during the seismic
 297 acquisition. The filter is convolved in the pre-stack (shot) domain as the periodicity of the bubble pulse
 298 is close to constant from shot to shot [Sargent *et al.*, 2011]. The source's notch effect was eliminated
 299 in the same domain, using a deterministic inverse filter constructed following the approach of Sargent *et*
 300 *al.* (2011). Although the deterministic inverse filters can be applied pre - stack, their periodicity and
 301 shape is tailored to the average observed notches observed in the stack amplitude spectrum. Similarly, the

302 receiver’s notch amplitude compensation is performed on a shot by shot basis by applying an automatic
 303 receiver’s deghosting filter in the f-x domain, after plane wave decomposition and separation of up-going
 304 and down-going waves [Amundsen, 1993].

305 The deep water environment of the segment (more than 2.5 Km depth from sea level) generates long
 306 path multiples that don’t interfere with the signal of the sedimentary sequence. As a result, we chose not
 307 to apply any demultiple techniques. After sorting shot gathers into Common Mid Point (CMP) gathers,
 308 several passes of manual velocity analysis and subsequent straight ray isotropic Kirchhoff pre – stack time
 309 migration (preSTM) are performed, aiming at building a smooth velocity field appropriate to produce flat
 310 image gathers. The final velocity model is also used for divergence correction to compensate for geometrical
 311 spreading. Before stacking, the flat time gathers underwent an outer trace mute to avoid any stretch effects
 312 at far offsets.

313 In the post - stack domain, random noise elimination is achieved by application of frequency - distance
 314 (f-x) deconvolution [Canales, 1984] and amplitude/phase inverse Q filter is applied to compensate for the
 315 attenuation during seismic wave propagation [Wang, 2002]. Time - variant bandpass filtering and cosmetic
 316 sea noise mute complete the processing of the profile in the time domain.

317 In figure 4, we present the comparison between images with (Fig. 4a, 4b) and without (Fig. 4c, 4d)
 318 notch compensation. The ghost free image shows optimum focusing and is characterized by a broadband
 319 amplitude spectrum (Fig. 4e). The retrieved frequency content improves the temporal resolution of
 320 the profile, which results to sharper seismic boundaries and by inference more constrain interpretation,
 321 especially at the shallow sedimentary sequence (arrows and curly brackets in Fig. 4b, 4d). Note, however,
 322 that the presence of basalts at around 4.5 seconds TWT [Maloney *et al.*, 2011] attenuates the high frequency
 323 content of the seismic energy [Maresh *et al.*, 2006] resulting in a poor reflectivity in the sub-basalt region.

324 3.3.2 Depth domain processing

325 Although the processing flow in the time domain yielded acceptably focused images, the 1D representation
 326 of the velocity model used in the time migration algorithm [Hubral, 1977; Black and Brzostowski, 1994]
 327 sets a limit to the precision of the velocity model building [Jones, 2010, 2012]. Thus, we opted to use
 328 the final version of the preSTM velocity field as a starting model to perform isotropic Kirchhoff pre -
 329 stack depth migration (preSDM) on the deghosted CMP gathers. As our well positions lie in an area with
 330 a relatively simple geological structure (Fig. 2b), we chose to run subsequent passes of vertical update
 331 [Deregowski *et al.*, 1990] to refine our input velocity field until acceptably flat CIG gathers were produced.

332 The resulted depth migrated images gathers are stretched back to time using the smoothed version of the
 333 final velocity field for filtering and cosmetic final residual moveout correction (RMO) and converted back
 334 to depth domain for stacking. This additional editing of velocity field assisted to constrain better the prior
 335 information for input to the Bayesian model and simultaneously assured that the velocity model is suitable
 336 to preSDM applications.

337 Even in an environment with subhorizontal layers and relatively simple subsurface structure like our
 338 area of interest, the preSTM and preSDM profiles show some structural differences, with the latter showing
 339 local sharpening of the faulted zones close to well locations (Fig. 5a, 5b). Furthermore, the amplitude
 340 compensation in the seismic gathers in time domain has generated a profile in depth domain with optimum
 341 spatial resolution and focusing (Fig. 5a, 5b). Thus, the application of pre-stack inverse filters serves as an
 342 amplitude shaping tool in both domains, in contrast with implementing deterministic post-stack inverse
 343 filters [Sargent *et al.*, 2011], which can produce flat amplitude spectrum and improved image resolution
 344 only in the time domain.

345 4. Results - Discussion

346 Using the final version of the $t_0 - V_{rms}$, $t_0 - V_{int}$. pairs as prior information for BRAINS along with the
 347 deghosted preSTM image gathers and performing BHM to reduce the parameter space, we calculate the
 348 posterior distribution of t_0 , V_{rms} , V_{int} and z for each CMP value and make uncertainty estimations for
 349 the variables of interest. Initially, the posterior mean V_{int} . field was used as input to the depth migration
 350 algorithm. A comparison between the images produced using the prior and posterior mean V_{int} fields is
 351 given in fig 6. The preSDM profiles don't indicate any major structural differences as the models used are
 352 nearly identical. This is a direct consequence of the Gaussian Process model used and the prior picks made,
 353 as the mean function in eq. (5) encodes the hyperbolic approximation of the seismic wave propagation.
 354 As the latter is also used to define the moveout trajectory for semblance spectrum calculation associated
 355 with hyperbolic events in CMP positions along a profile, the closest the prior $t_0 - V_{rms}$ or $t_0 - V_{int}$. picks
 356 are to the local maxima semblance value, the less difference will be observed between prior and posterior
 357 mean models and by inference depth images.

358 Differences are resolved after subtracting the posterior mean preSDM image (Fig. 6b) from its prior
 359 equivalent (Fig. 6a), resulting in a structural difference plot (Fig. 6c, Fig. 6d). The images' dissimilar
 360 features are now emphasized, indicating regions of differential depth shift. As the migration algorithm
 361 repositions the time signal to the depth domain in a top - down basis, the cumulative differences of

362 velocity field with respect to depth get larger and map to more pronounced depth image shifts. Note that
 363 as the velocity fields show minor differences, this effect generates only a vertical structural stretch with no
 364 resolvable lateral structural changes.

365 In terms of depth predictions, although we used an isotropic approximation of preSDM, the tie with the
 366 borehole information is acceptable with a misfit of approximately 4 % (21 m) at the glauconitic sandstones
 367 level (Fig. 7a, 7b). The large misfit at the bottom shales level is attributed to the indistinct reflectivity
 368 boundary between limestones and shales (Fig. 7a, 7b). Note, however, that the observed depths from
 369 DSDP-258 are consistent with the $\pm 2\sigma$ credibility intervals. This result reassures us that our posterior
 370 mean velocity field is a good representation of the local velocity field and, by inference, can be used to
 371 make predictions about the depths to horizons in the new well locations (Fig. 7a, 7b).

372 The uncertainty quantification not only results in a numerical estimation of depth values for key hori-
 373 zons, but can be also used to generate a set of probabilistic images by sampling $V_{int.}$ values from the
 374 posterior distribution and using the latter as input to preSDM algorithm. In figure 7c, we present a num-
 375 ber of structural difference plots, produced by subtracting each resulted preSDM image realization, derived
 376 using a probabilistic velocity field, from the posterior mean image. The plots display a number of probable
 377 depth and shape positions for geological boundaries of interest, in accordance with the differences between
 378 the sampled velocity fields and the posterior mean velocity field (Fig 7c(i), 7c(iii) $\pm 2\sigma$ end members for
 379 posterior black shales velocity, 7c(iv), 7c(v), 7c(vi) randomly generated values for all velocity layers, 7c(ii)
 380 posterior mean image). In positions where the differences are closer to extreme values, the local image
 381 features start changing in shape (localised red maxima in 7c(iii), 7c(iv)).

382 The randomly generated values, bounded by the $\pm 2\sigma$ credibility intervals for every CMP position and
 383 every velocity layer, incorporate a confidence measure associated to each picked pair which is a combination
 384 of the observed data (amplitude values A_{ij} , recorded travel time $T_{ij}^{(r)}$, distance X_j), and prior picks
 385 positions. Thus, the retrieved vertical pattern of blue (negative) and red (positive) regions in the normalized
 386 velocity difference plots of figure 7c approximates the Gaussian Process pattern depicted in figure 3c, where
 387 the $\pm 2\sigma$ curves, along a velocity layer, show decreased uncertainty close to the prior picked CMP positions
 388 and increased between them. These regions have a spacing of approximately 50 CMPs positions, driven
 389 by the velocity picking spacing used to generate the prior velocity model for time and depth migration
 390 (Table 2). We expect that the mapping of the uncertain nature of velocity models to image realizations,
 391 especially in areas with complex geological structures such as salt diapirs or basalt intrusions, is critical to
 392 constrain better the most probable interpretations and risk.

393 The observed misfit between the modelled mean and true depths at the glauconitic sandstones level
 394 can be primarily attributed to the isotropic approximation of BRAINS and the migration algorithm used.
 395 As described in expressions (5), (6) and (7), the Gaussian process emulator does not include an explicit
 396 representation of epsilon (ϵ) and delta (δ) anisotropic parameters [Thomsen, 1986], therefore these terms
 397 are not statistically quantified as an output from the model. The uncertainty related with anisotropic
 398 conditions is integrated in our system into the model discrepancy term which value is set accordingly to
 399 accommodate the mismatch in the predicted depths and observed data, driven primarily by excluding
 400 Thomsen's ϵ and δ parameters. This approach was chosen in order to avoid narrow posterior variances
 401 which would indicate overconfident depths predictions for the drilling targets, predictions that couldn't
 402 be supported for the result extracted using an isotropic depth migration algorithm alone, without the
 403 confirmation from independent observations (well logs).

404 Although indirect, this compensation of the anisotropic parameters through a unified discrepancy term
 405 can be considered as the optimum solution in our system. Firstly, the lack of any wireline log information
 406 concerning seismic velocities does not facilitate the process of anisotropic velocity model building as the
 407 true velocity values could be implemented to better constrain the prior information in our model and simul-
 408 taneously be used as a starting point for higher order NMO correction (4^{th} order correction, η parameter).
 409 Furthermore, due to the uncertain tie between the observed reflectivity in the final preSTM / preSDM
 410 images and the lithological boundaries (especially at the boundary between limestones to black shales),
 411 any scaling of the target horizons to match the observed depths [Davies *et al.*, 1974] using an inferred δ
 412 parameter value is impractical and contains the risk of assigning observed reflectivities to incorrect geolog-
 413 ical boundaries and hence depths. As a result, trying to infer the anisotropic parameters and provide their
 414 uncertainty estimations, without any well control, was a task prone to uncertainties that could compromise
 415 the predictions of velocities and depths for the horizons of interest.

416 However, there is an additional, more subtle reason that justifies our approach. It has been shown [Al-
 417 Chalabi, 2014], that the inclusion of a 4^{th} order term during NMO correction (estimation of η parameter)
 418 is associated with a large increase in the observed variance compared to the simpler 2^{nd} order hyperbolic
 419 approximation mainly due to the strong anti - correlated nature between V_{nmo} and η variables. This
 420 result indicates, that an anisotropic approach during the velocity analysis stage combined with anisotropic
 421 migration algorithms, although may result to better focusing of the final image and possibly better prior
 422 / posterior mean depth results, does not lead to a better uncertainty quantification of velocity values.

423 5. Conclusion

424 We have presented a method to quantify the uncertainty of depths and related values in seismic reflection
 425 data processing. Our seismic reflection processing strategy was separated into two distinct parts. First,
 426 we aimed to improve the temporal and spatial resolution of the region close to the planned well locations
 427 by performing source’s and receiver’s notch compensation in the pre - stack domain. Then, we focused
 428 on the velocity model building in the time and depth domain in order to generate well focused images
 429 and constraint prior information for input to the BRAINS model. By using Gaussian Process emulators
 430 conjointly with iterative Bayesian History Matching (BHM), we managed to retrieve the depths of the
 431 key horizons as known from DSDP–258 borehole and make predictions about the expected depths of same
 432 horizons for wells 4B, 4C respectively.

433 As the probabilistic approach results in a distribution estimation for $V_{int.}$, we generated sets of new
 434 velocity models and perform preSDM to produce different image realizations. In this way, we were able to
 435 map differences in velocity models to differences in image features for our horizons of interest.

436 The GP emulators are deliberately parametrized to exclude explicit uncertainty estimations for anisotropic
 437 parameters (ϵ, δ). Instead, the anisotropic effects during seismic wave propagation are unified in the model
 438 discrepancy term (ϵ_{ij} or σ_{n_i}), a term which is easier to tune and with the synergy of prior information of
 439 picked $\{V_{rms}, t_0\}$ or $\{V_{int.}, t_0\}$ pairs, it allows constrained posterior results. The inclusion of the anisotropic
 440 terms as independent variables in our model along with their explicit uncertainty estimation, would require
 441 well log information concerning true seismic velocities and also well to seismic tie to unambiguously map
 442 observed reflectivities from seismic data to lithological boundaries. Even in that case, their incorporation
 443 could pose problems concerning the robustness of their uncertainty estimations, as in time domain the
 444 terms are accessed solely through η parameter [*Alkhalifah & Tsvankin, 1995; Alkhalifah, 1997*], a term that
 445 is strongly coupled to the small - offset moveout velocity (V_{nmo}), that a useful uncertainty estimation is in
 446 question.

447 The statistical model described in this paper is based on the discrete layer velocity model representation
 448 and can be easily coupled with a layer – based tomographic inversion scheme. The challenge will be to
 449 incorporate an analogous model to gridded or hybrid velocity model representations [*Jones et al., 2007*]
 450 for complex geological structures, where the velocity regime is controlled by a combination of vertical
 451 compaction gradients and sharp velocity contrasts.

452 **Acknowledgments**

453 The seismic reflection profile S310-07 was provided by Geoscience Australia. GNS Globe Claritas software
454 was used for seismic reflection processing; PGS Nucleus modelling package was used to compute theoretical
455 source signature and Matlab Mathworks for statistical analysis; Seismic Un*x [Cohen and Stockwell, 2010]
456 was used to plot sections for publication.

457 **References**

- 458 Abrahamsen, P., Omre, H. & Lia, O. (1991). Stochastic models for seismic depth conversion of geo-
459 logical horizons. *SPE* 23138, 329–341. <https://doi.org/10.2118/23138-MS>.
- 460 Al-Chalabi, M. (1994). Seismic velocities - A critique. *First Break* 12, 589–596. doi : 10.3997/1365-
461 2397.1994036.
- 462 Al-Chalabi, M. (2014). Principles of Seismic Velocities and Time-to-Depth Conversion. *EAGE Publi-*
463 *cations*.
- 464 Alkhalifah, T. & Tsvankin. (1995). Velocity analysis for transversely isotropic media. *Geophysics* 60,
465 1654–1660. doi : 10.1190/1.1443888.
- 466 Alkhalifah, T. (1997). Velocity analysis using nonhyperbolic moveout in transversely isotropic media.
467 *Geophysics* 62, 1839–1854. doi : 10.1190/1.1444285.
- 468 Amundsen, L. (1993). Wavenumber-based filtering of marine point-source data. *Geophysics* 58, 1335-
469 1348. doi : 10.1190/1.1443516.
- 470 Andrianakis, I., Vernon, I.R., McCreesh, N., McKinley, J.T., Oakley, J.E., Nsubuga, R.N., Goldstein,
471 M. & White, R.G. (2015). Bayesian History Matching of Complex Infectious Disease Models Using
472 Emulation: A Tutorial and a Case Study on HIV in Uganda. *PLOS Computational Biology* 11,
473 e1003968.
- 474 Bickel, S. H. (1990). Velocity-depth ambiguity of reflection traveltimes. *Geophysics* 55, 266–276. doi :
475 10.1190/1.1442834.
- 476 Black, J. L. & Brzostowski M.A. (1994). Systematics of time-migration errors. *Geophysics* 59, 1419-
477 1434. doi : 10.1190/1.1443699.
- 478 Borissova, I. (2002). Geological framework of the Naturaliste Plateau. *Geoscience Australia Record*
479 2002/20, 2002.
- 480 Bradshaw, B.E., Rollet, N., Totterdell, J.M. & Borissova, I., (2003). A revised structural framework
481 for frontier basins on the southern and southwestern Australian continental margin. *Geoscience*
482 *Australia Record*.

- 483 Caiado, C.C.S., Hobbs, R.W. & Goldstein, M. (2012). Bayesian Strategies to Assess Uncertainty in
484 Velocity Models. *Bayesian Analysis* 7, 211–234. doi : 10.1214/12-BA707.
- 485 Caiado, C.C.S. & Goldstein, M. (2015). Bayesian uncertainty analysis for complex physical systems
486 modelled by computer simulators with applications to tipping points. *Communications in Nonlinear
487 Science and Numerical Simulation* 26, 123–126. <http://dx.doi.org/10.1016/j.cnsns.2015.02.006>.
- 488 Canales, L. (1984). Random noise reduction: SEG Technical Program, Expanded Abstracts, 525–527.
489 doi: 10.1190/1.1894168.
- 490 Chen, J. and Schuster, G.T. (1999). Resolution limits of migrated images. *Geophysics* 64, 1046-1053.
491 doi: 10.1190/1.1444612.
- 492 Chitu, D.A., Al-Ali, M.N. & Verschuur, D.J. (2008). Assessing estimated velocity-depth models: Find-
493 ing error bars in tomographic inversion. *Geophysics* 73, VE223–VE233. doi: 10.1190/1.2951469.
- 494 Cohen, J. K. & Stockwell, Jr. J. W. (2010). CWP/SU: Seismic Un*x Release No. 42: an open source
495 software package for seismic research and processing, Center for Wave Phenomena, Colorado School
496 of Mines.
- 497 Craig, P.S., Goldstein, M, Scheult, A.H. & Smith, J.A. (1997). Pressure matching for hydrocarbon
498 reservoirs: a case study in the use of Bayes linear strategies for large computer experiments (with
499 discussion). In: Gatsonis, C., Hodges, J.S., Kass, R.E., McCulloch, R.E., Rossi, P. and Singpurwalla,
500 N.D., eds. *Case Studies in Bayesian Statistics* III, 37-93. Springer-Verlag. doi: 10.1007/978-1-4612-
501 2290-3-2.
- 502 Cumming, J.A. & Goldstein, M. (2009). Bayes linear uncertainty analysis for oil reservoirs based on
503 multiscale computer experiments. In: O’ Hagan, A. and West, M., eds. *The Oxford Handbook of
504 Applied Bayesian Analysis*, 241–270, Oxford, UK: Oxford University Press.
- 505 Davies, T. A., B. P. Luyendyk, et al. (1974). Shipboard site reports, site 258. Initial reports of the
506 Deep Sea Drilling Project, Leg 26, in T. A. Davies, B. P. Luyendyk, et al., eds., Initial Reports of
507 the Deep Sea Drilling Project. *U.S. Government Printing Office* 26, 359–414.
- 508 Deregowski, S. M. (1990). Common-offset migrations and velocity analysis. *First Break* 8, 225–234.
509 doi : 10.3997/1365-2397.1990011.

- 510 Direen, N.G., Borissova, I., Stagg, H.M.J., Colwell, J.B. & Symonds, P.A. (2007). Nature of the
511 continent-ocean transition zone along the southern Australian continental margin: a comparison of
512 the Naturaliste Plateau, SW Australia, and the central Great Australian Bight sectors, in: *Imaging,
513 mapping and modelling continental lithosphere extension and breakup*, edited by: Karner, G. D.,
514 Manatschal, G., and Pinheiro, L. M., Geological Society (London) Special Publication, 282, 235–
515 261, 2007.
- 516 Dix, C.H. (1955). Seismic Velocities from Surface Measurements. *Geophysics* 20, 68–86. doi :
517 10.1190/1.1438126.
- 518 Hawkins, K., Leggott, R., Williams, G. & Kat, H. (2001). Addressing anisotropy in 3-D prestack
519 depth migration: A case study from the Southern North Sea. *The Leading Edge* 20, 528–543. doi :
520 10.1190/1.1438988.
- 521 Hubral, P. (1977). Time migration – Some ray theoretical aspects. *Geophysical Prospecting* 25, 738–
522 745. doi : 10.1111/j.1365-2478.1977.tb01200.x.
- 523 Jones, I.F., Surgue, M.J. & Hardy, P.B. (2007). Hybrid gridded tomography. *First Break*, 25(4), 35–41.
- 524 Jones, I.F., (2010). An Introduction to: Velocity Model Building. *EAGE Publications*, The Nether-
525 lands, 295 p.
- 526 Jones, I.F., (2012). Tutorial: Incorporating near-surface velocity anomalies in pre-stack depth migra-
527 tion models. *First Break*, 30, 47–58. doi : 10.3997/1365-2397.2011041.
- 528 Jones, I.F., (2014). Estimating subsurface parameter fields for seismic migration: Velocity model build-
529 ing. *Encyclopedia of Exploration Geophysics*, U1-1-U1-24. doi: 10.1190/1.9781560803027.entry3.
- 530 Journel, A.G. & Huijbregts, C.H. (1978). Mining Geostatistics. *Academic Press, London*, 600 p.
- 531 Ko, J. & Fox, D. (2009). GP-BayesFilters: Bayesian filtering using Gaussian process prediction and
532 observation models. *Autonomous Robots* 27, 75–90. doi : 10.1007/s10514-009-9119-x.
- 533 Kosloff, D.D. & Sudman Y. (2002). Uncertainty in determining interval velocities from surface reflec-
534 tion seismic data. *Geophysics* 67, 952–963. doi : 10.1190/1.1484537.
- 535 Kuypers, M. M. M., Pancost, R. D. & Damste, J. S. S. (1999). A large and abrupt fall in atmospheric
536 CO₂ concentration during Cretaceous times. *Nature* 399, 342–345. doi: 10.1038/20659.

- 537 Landa, E. (1991). Interpretation of velocity estimates from coherency inversion. *Geophysics* 56, 1377–
538 1383. doi : 10.1190/1.1443157.
- 539 Lewis, L., Caers, J. & Sava, P. (2015). Assessing seismic uncertainty via geostatistical velocity-model
540 perturbation and image registration: An application to subsalt imaging. *The Leading Edge* 34,
541 1064–1066, 1068–1070. doi : 10.1190/tle34091064.1.
- 542 Lines, L. (1993). Ambiguity in analysis of velocity and depth. *Geophysics* 58, 596–597. doi :
543 10.1190/1.1443443.
- 544 Maloney, D., Sargent, C., Direen, N.G., Hobbs, R.W. & Grocke, D.R. (2011). Re-evaluation of the
545 Mentelle Basin, a polyphase rifted margin basin, offshore southwest Australia: new insights from
546 integrated regional seismic datasets. *Solid Earth* 2, 107-123. doi:10.5194/se-2-107-2011.
- 547 Maresh, J., White, R.S., Hobbs, R.W. & Smallwood J.R. (2006). Seismic attenuation of Atlantic
548 margin basalts: Observations and modeling. *Geophysics* 71, B211–B221. doi: 10.1190/1.2335875.
- 549 Matheron, G. (1973). The Intrinsic Random Functions and Their Applications. *Advances in Applied*
550 *Probability* 5, 439-468. doi : 10.2307/1425829.
- 551 Messud, J., Reinier, M., Prigent, H., Guillaume, P., Colou, T. & Masclet, S. (2017). Extracting
552 seismic uncertainties from tomographic velocity inversion and their use in reservoir risk analysis.
553 *The Leading Edge* 36, 127132. doi: 10.1190/tle36020127.1.
- 554 Neidell, N.S. & Taner M.T. (1971). Semblance and other coherency measures for multichannel data.
555 *Geophysics* 63, 482–497 doi : 10.1190/1.1440186.
- 556 O’Hagan, A. (2006). Bayesian analysis of computer code outputs: A tutorial. *Reliability engineering*
557 *and system safety* 91, 1290–1300 doi : 10.1016/j.res.2005.11.025.
- 558 Powell, C.M., Roots, S.R. & Veevers, J.J. (1988). Pre-breakup continental extension in East Gond-
559 wanaland and the early opening of the eastern Indian Ocean. *Tectonophysics* 155, 261–283
560 doi:10.1016/0040-1951(88)90269-7
- 561 Pukelsheim, F. (1994). The Three Sigma Rule. *The American Statistician* 48, 88–91
562 doi:10.2307/2684253.
- 563 Rasmussen, C. E. & Williams, C. K. I. (2006). Gaussian Processes for Machine Learning. *MIT Press,*
564 *Cambridge*, 245 p.

- 565 Ripley, B.D. (1991). *Statistical Inference for Spatial Processes*. Cambridge University Press, 148 p.
- 566 Royer, J.Y. & Coffin, M.F. (1992). Jurassic to Eocene plate tectonic reconstructions in the Kergue-
567 len Plateau region. In: S.W. Wise Jr. and R. Schlich (Editors) *Proceedings of the Ocean Drilling*
568 *Program, Scientific Results* 120, 917-928.
- 569 Sargent, C., Hobbs, R.W. & Grocke, D.R. (2011). Improving the interpretability of air-gun seismic
570 reflection data using deterministic filters: A case history from offshore Cape Leeuwin, southwest
571 Australia. *Geophysics* 76, B113B125. doi : 10.1190/1.3554396.
- 572 Thomsen, L. (1986). Weak elastic anisotropy. *Geophysics* 51, 1954–1699. doi : 10.1190/1.1442051.
- 573 Tieman, H. J. (1994). Investigating the velocity-depth ambiguity of reflection traveltimes. *Geophysics*
574 59, 1763–1773. doi : 10.1190/1.1443563.
- 575 Vernon, I., Goldstein, M. & Bower, R. G. (2010). Galaxy Formation: a Bayesian Uncertainty Analysis.
576 *Bayesian Analysis* 5, 619–670. doi : 0.1214/10-BA524.
- 577 Wang, Y., (2002). A stable and efficient approach of inverse Q filtering. *Geophysics* 67, 657-663. doi:
578 10.1190/1.1468627.

Table 1: Acquisition specifications for line S310-07

Parameter	Value
Source type	Tuned point-source air-gun array
Gun type	Bolt 1500LL air guns
Nominal source volume	70.3 L (4290 cu in)
Nominal source pressure	13.7 Mpa (2000 psi)
Nominal source depth	7 \pm 1 m
Shotpoint interval	37.5 m
Streamer type	Sercel Seal Solid
Number	1
Streamer Length	8100 m
Number of groups	648
Group length	12.5
Nominal streamer depth	10 \pm 1 m
Nominal inline offset	94
Recording system	Sercel SEAL v5.2
Record length	12 s
Sample interval	2 ms
Low-cut filter/ slope	2Hz at 6dB/Oct, Digital Low-Cut: OFF
High-cut filter/ slope	200Hz at 370 dB/Oct
Recording format	SEGD 8058 rev.1 32bbit IEEE

Table 2: Processing sequence applied to seismic line S310-07 (time domain)

S310-07
Reformat and geometry import - CDP spacing = 6.25 m - Nominal CDP fold = 108
Instrument delay correction = 100 ms, Source-Receiver datuming
Zero phase low cut Butterworth filter 4 Hz, 18 db/octave
Modelled debubble inverse filter (shot gathers)
Deterministic inverse filter for source's notch compensation (shot gathers) derived from post - stack amplitude spectrum
Receiver's notch compensation in f - x domain (shot gathers)
CMP Sorting and Velocity analysis (every 312.5 m / 50 CMPs)
Straight ray isotropic Kirchhoff Pre Stack Time Migration (PreSTM)
Spherical Divergence Correction
Outer Trace Mute and Stack
Time variant zero phase Butterworth filter: 10-20-100-125 at seabed (sb), 10-20-100-125 at sb + 0.3 s, 8-15-100,120 at sb + 0.6 s, 5-10-90-110 at sb + 0.9 s, 3-8-50-70 at sb + 2.5 s
Frequency - distance (f-x) deconvolution for random noise attenuation
Amplitude-phase Inverse Q compensation = 200
Cosmetic sea noise mute

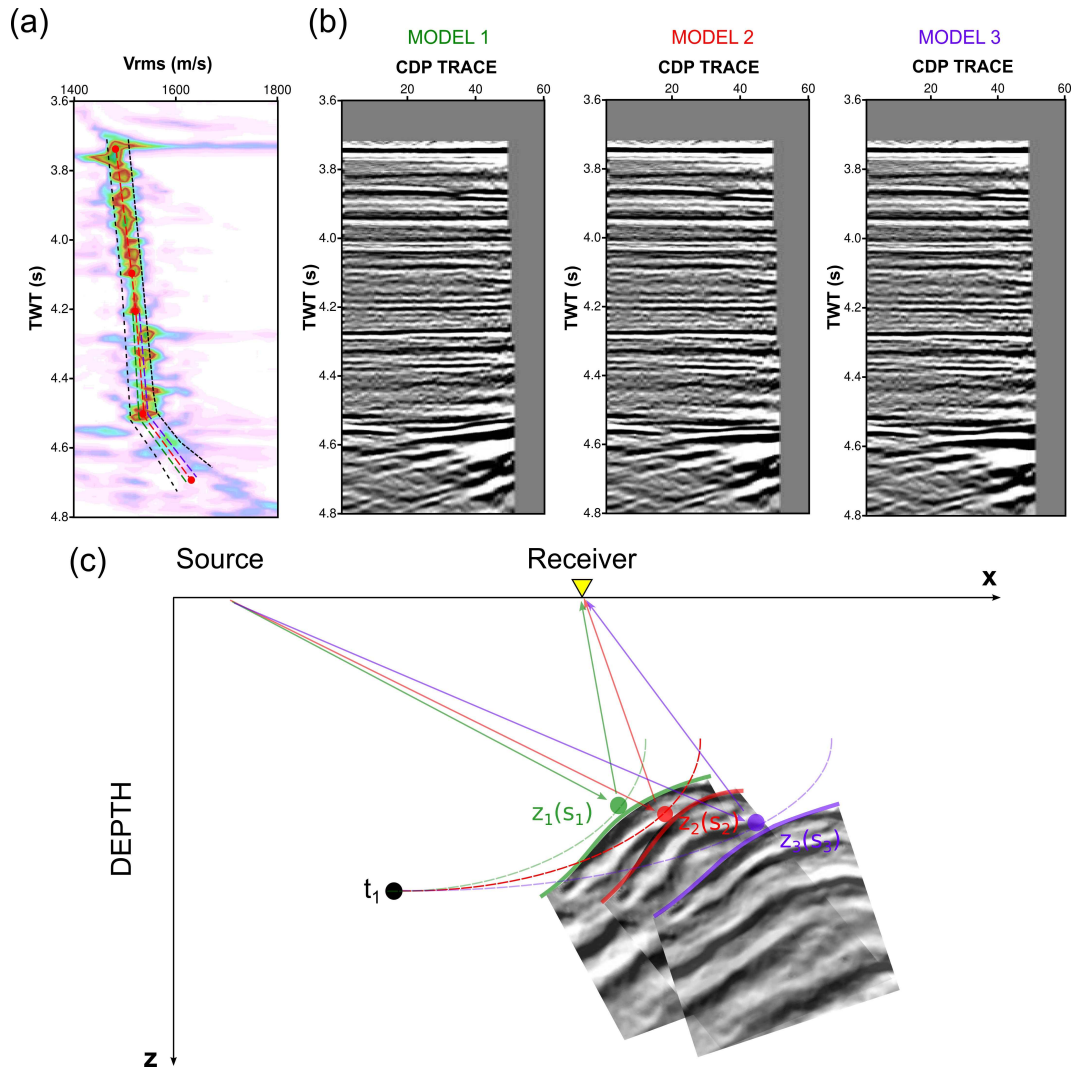


Figure 1: Uncertainty in velocity model building. (a): The semblance spectrum as a velocity estimation tool gives robust time - velocity picks for the shallow parts, but for later times the envelope of possible picked pairs (dashed black lines) becomes broader due to attenuation effects and poor depth to offset ratio. (b): The 3 velocity models (under colors red, purple, green), having differences only after 4.2 seconds TWT, result in equally flat gathers but can lead to different shapes and depths for the same horizons after pre - stack depth migration (preSDM). (c): Tomographic inversion in the depth migration domain preserves the observed invariant time (t_1) of an arrival by using different values of thickness (z) and slowness (s). As a consequence, the mapping from time to depth can result in slightly different realizations of the same boundary. (panel c, modified from Jones, 2010, Fig. 5.23).

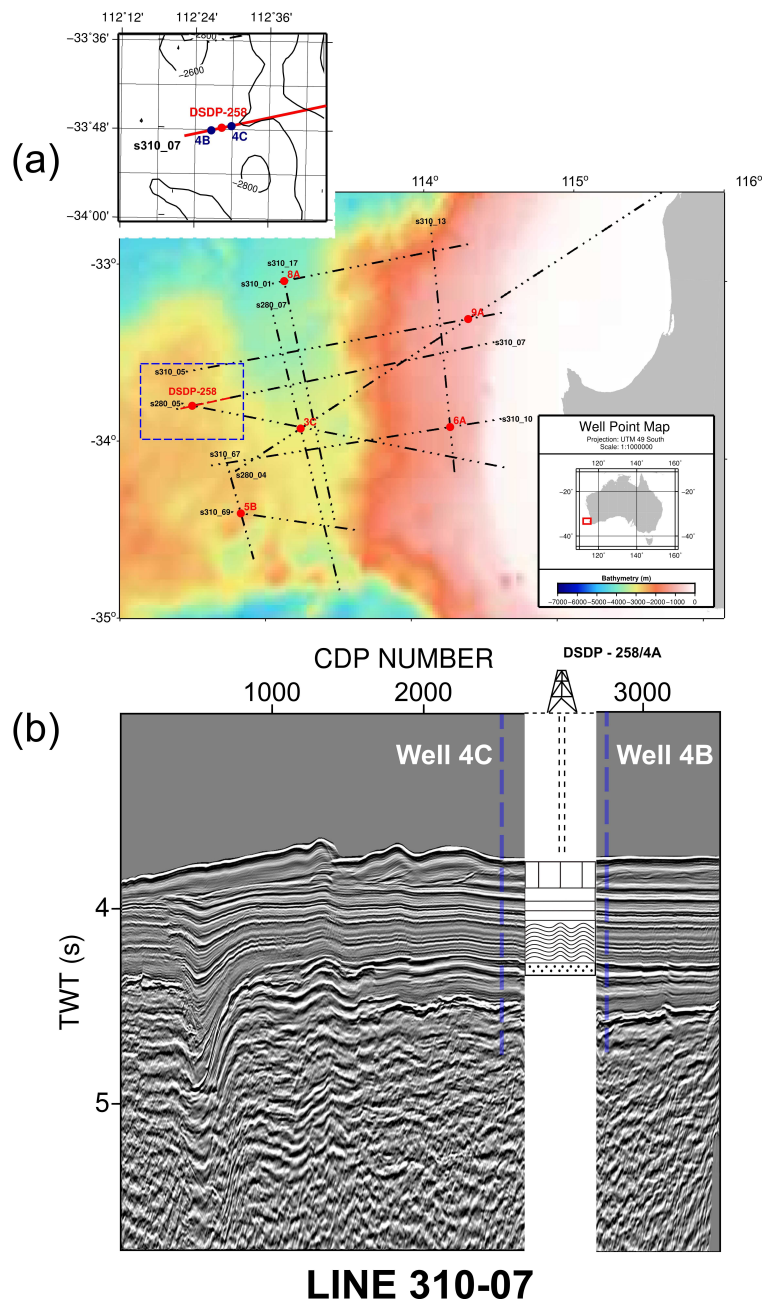


Figure 2: (a): Bathymetric map of Mentelle Basin. The positions of 2D seismic lines (dashed black lines) and planned well locations (red circles) are shown. Red dashed line represent the segment reprocessed in this paper. Insert, the two new planned well positions adjacent to DSDP - 258 are marked in blue (4B - 4C). (b): DSDP - 258 borehole tied to ghost free Pre - Stack time migrated (preSTM) profile S310-07. In the lithological interpretation: vertical hatching carbonate oozes; horizontal hatching chalks; wavy hatching black shales; black stipples glauconitic sands. Blue dashed lines intersecting profile S310-07, indicate the positions of Wells 4C, 4B respectively.

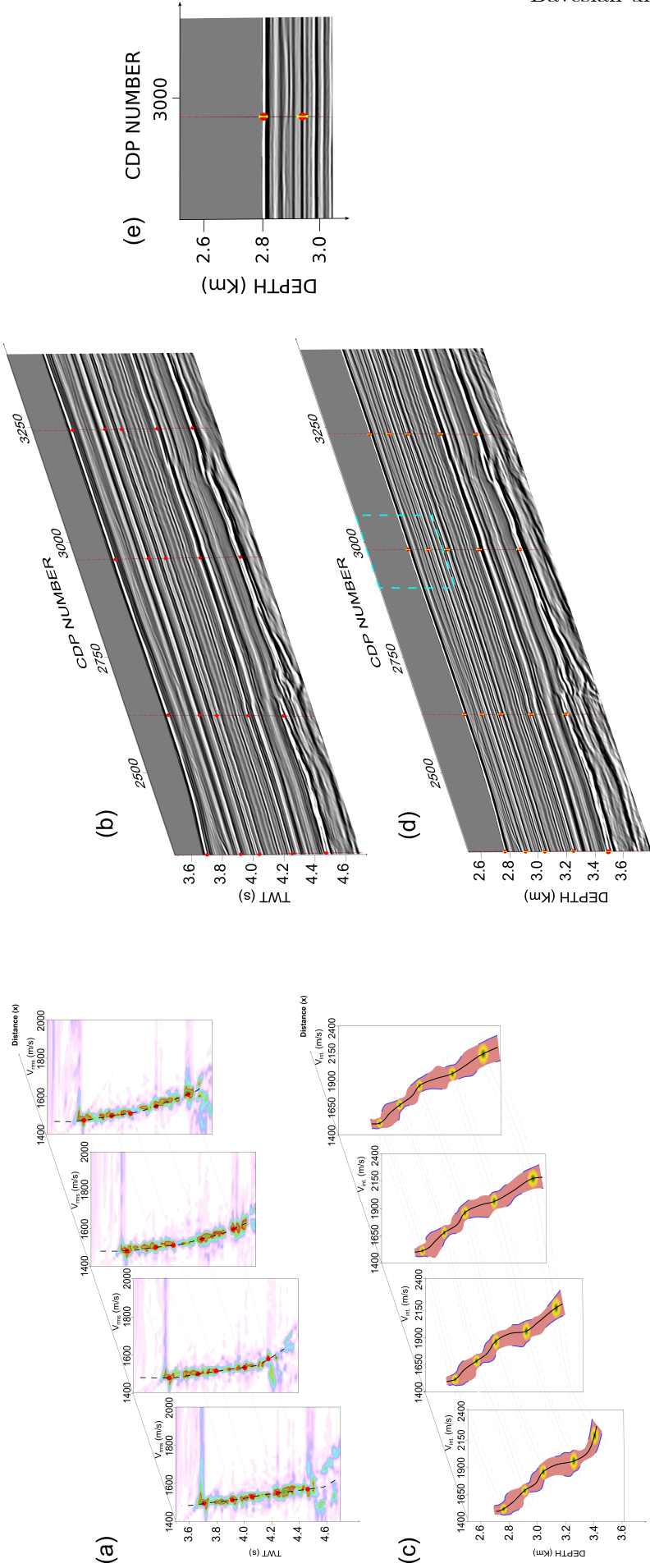


Figure 3: Schematic representation of the application of Gaussian Process and Bayesian History Matching (BHM) in seismic reflection data. (a): a number of semblance spectrum plots associated with CMP positions along a preSTM profile shown in (b). The $T_0 - V_{rms}$ pairs, at semblance maxima (red circles), can be picked to follow seismic boundaries. Between analysis locations, the $T_0 - V_{rms}$ pairs are linearly interpolated (dashed gray lines) but don't incorporate any uncertainty estimation. (c): Using GP and BHM, the semblance spectrum can be substituted by an implausibility map. Trends represent the implausibility map for $Z - V_{int}$ pairs, the latter being spatially linked with the preSDM figure shown in (d). Green regions, at prior picks, indicate low implausibility levels (most probable pairs) and red and yellow higher levels of implausibility. The user defined picks, both in depth and velocity domain, are bounded by the $\pm 2\sigma$ posterior uncertainty curves (blue dashed curves) with the posterior mean function (black solid curves) passing through the regions of lowest implausibility. The probabilistic approach gives an uncertainty estimation for each layer along a profile in positions where we don't provide prior information to define a depth velocity volume (black solid curves along layers, posterior mean function - blue dashed curves along layers, posterior $\pm 2\sigma$). The yellow bars on the preSDM image (d) represent the depth uncertainty from our analysis. (e): Zoomed panel of the cyan dashed box in (d).

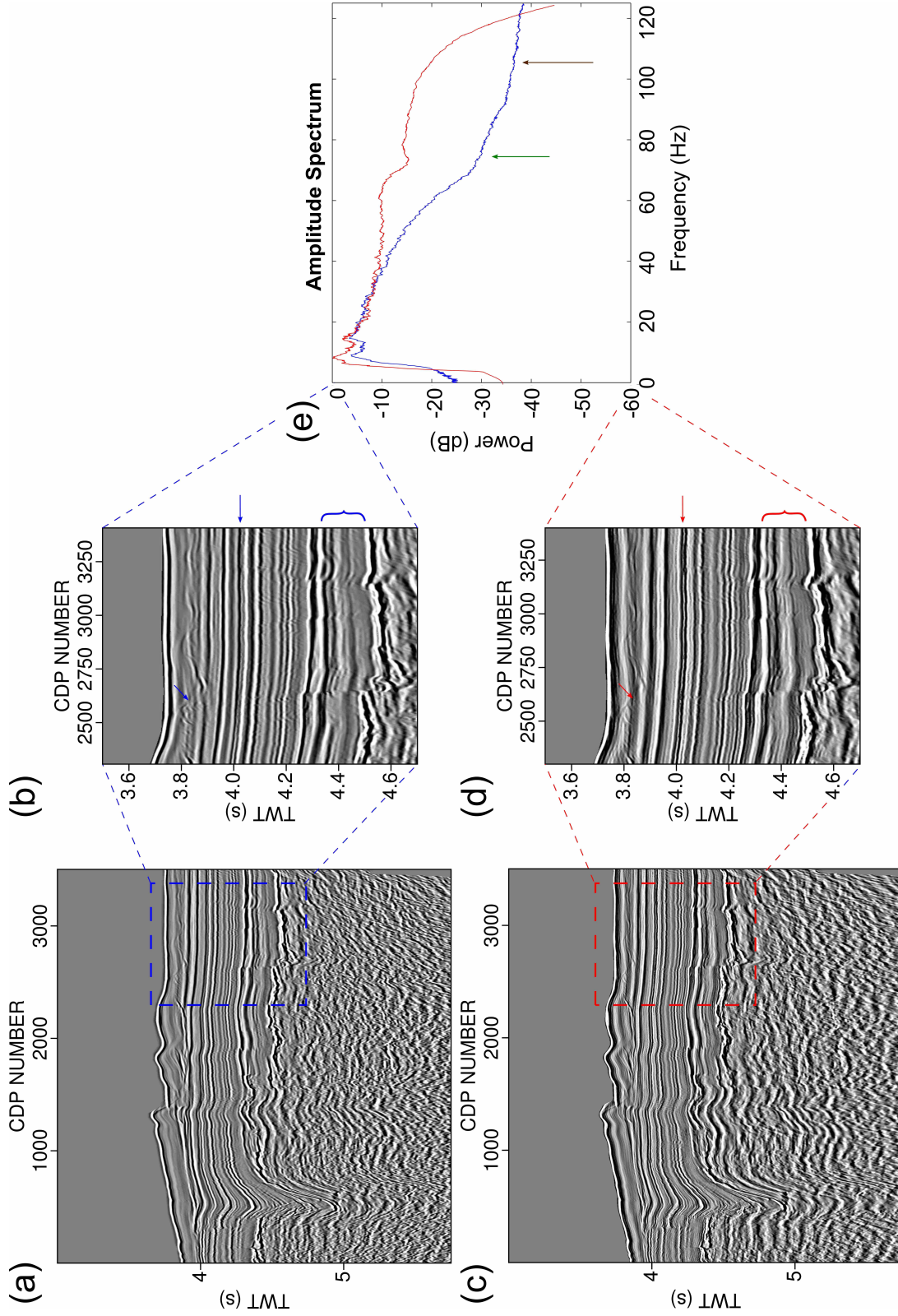


Figure 4: Comparison between preSTM images with and without notch compensation. (a), (b): PreSTM profile and zoomed panel close to well locations produced following the processing root of Table 2 without any notch elimination. (c), (d): Same as in (a), (b) but with source's and receiver's notches elimination performed in blue and red arrows respectively. (e): Amplitude spectra of the images (blue from panel (b), red from panel (d)) showing the retrieved amplitude after compensating for source and receiver notches (green and brown arrows).

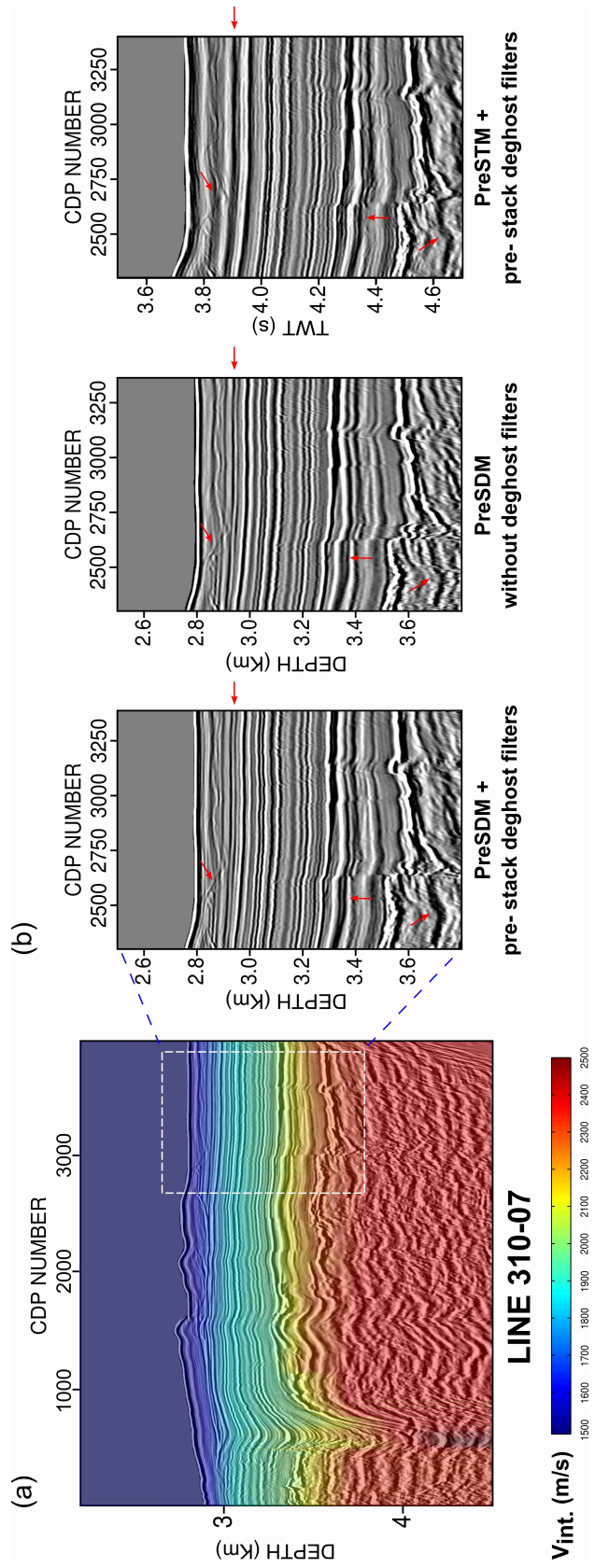


Figure 5: (a): PreSDM image generated using the final version (prior) V_{int} . velocity field as input to migration algorithm (superimposed). (b): preSDM/preSTM images with and without prestack amplitude shaping. Red arrows indicate the most pronounced structural and spatial / temporal differences, in the shallowest and deeper parts of the images, emerged after application of depth migration and inverse filtering in the pre – stack domain. Although the geological structure is relatively simple, the image differences are locally considerable indicating the need for optimum elimination of ghost notches and velocity refinement through an iterative preSDM loop to better constraint the prior velocity information.

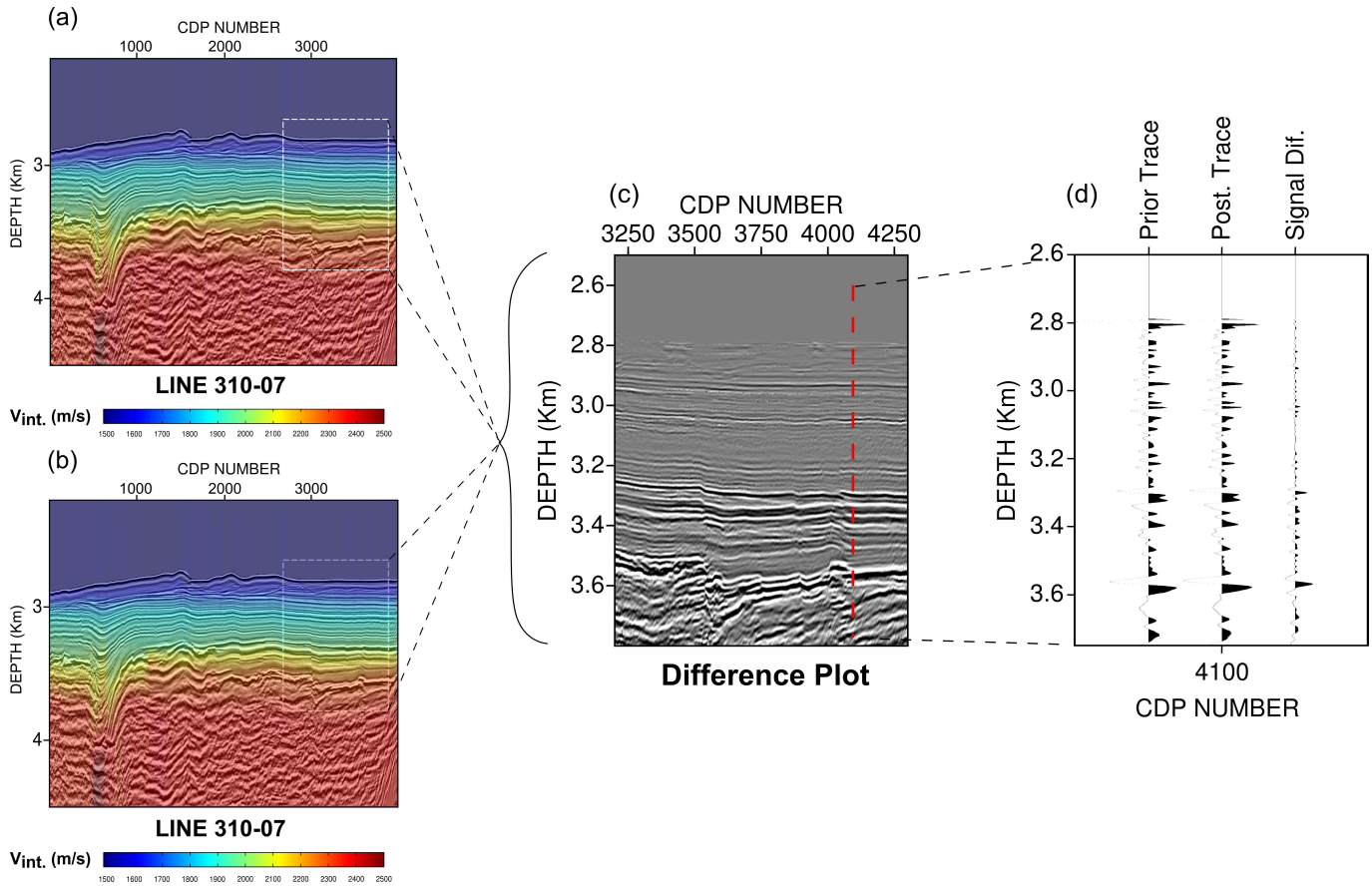


Figure 6: Comparison between prior and posterior mean preSDM images. (a): Image generated using the prior V_{int} velocity field (superimposed). (b): Image using the posterior mean V_{int} velocity field (superimposed). (c): The velocity fields and images don't present any significant differences, therefore possible structural changes can become apparent after using a structural difference plot, which is the result of subtracting the posterior mean image (b) from prior image (a). The image features' changes are more pronounced in the deeper parts of the profile as a direct consequence of top – down reposition of the signal. (d): Example of signal difference extracted from a depth window of CDP number 4100 (red dashed line in panel (c)), as calculated by subtracting the posterior from the prior signal.

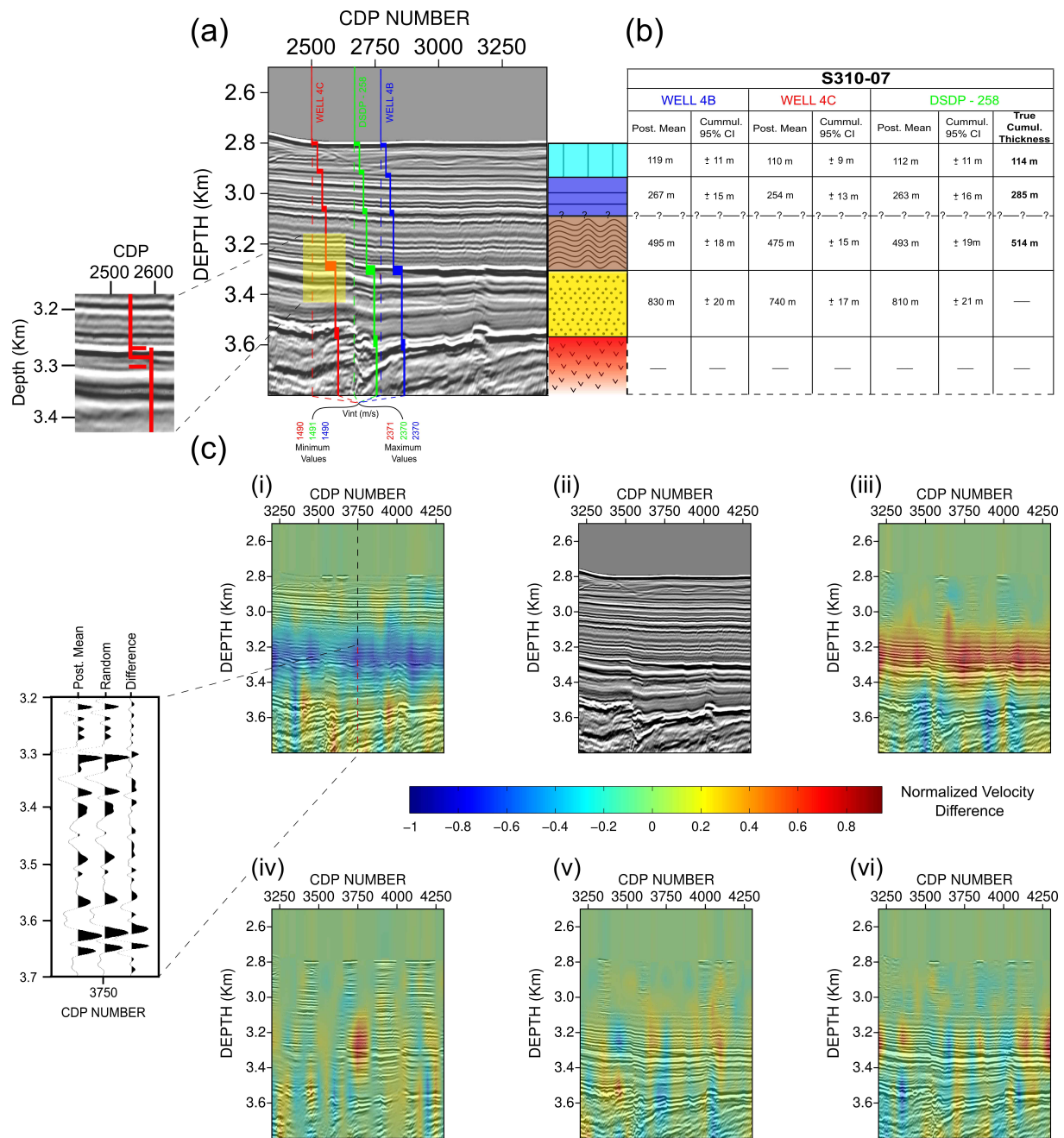


Figure 7: Posterior depth results and probabilistic imaging: (a): PreSDM image for S310-07 profile. Dashed vertical lines represent the wells' locations, with the posterior range of interval velocity/depth values for each layer superimposed as filled coloured regions (red, green, blue colours for Well 4C, DSDP - 258 (Well 4A) and Well 4B respectively). Zoomed panel shows the region associated with the yellow rectangle as an example of the posterior mean and $\pm 2\sigma$ trends for top glauconitic sandstones (red solid trend in zoom represent posterior mean values, dashed lines in zoom the $\pm 2\sigma$ intervals respectively). (b): The predictions for the cumulative thickness of drilling targets for each well location, associated with the lithological interpretation from figure 2. (c): A number of preSDM structural difference plots, using $V_{int.}$ sampled from the posterior distribution. The superimposed coloured map represents the normalized difference between the randomly generated $V_{int.}$ velocity fields used to produce each profile and the posterior mean. Panels c(i), c(iii) demonstrate the $\pm 2\sigma$ end members for black shales velocity layer with the remaining layers preset to take random values from the posterior distribution. Zoomed panel from c(i) shows how the difference plot is generated. Figure c(ii) same as in (a). Panels c(iv), c(v), c(vi) represent fields allowed to span the total $V_{int.}$ space of the posterior distribution.

579 Appendix A: Bayesian Models and Gaussian Process in seismic reflection

580 In the following, we will briefly describe the 1D and 2D Gaussian Process emulators used. See [Caiado et
581 al., 2012] for a full description of the models.

582 A.1 1D emulator

583 Suppose a discretized subsurface model, with a finite number of interfaces b_i and a given array of source –
584 receiver pairs, S_j and R_j , containing m pairs. All the pairs are symmetrically placed around a Common
585 Mid Point (CMP), with X_j being the distance between S_j and R_j . As the medium is discretized, we can
586 associate to every layer i , a two way travel time T_{0_i} with its time increment ΔT_{0_i} , a root-mean-square
587 velocity V_{rms_i} with its increment ΔV_{rms_i} and a thickness ΔZ_i . Furthermore, let T_{ij} be the real time for a
588 wave ray to propagate from seismic source S_j to detector R_j , by refracting at interfaces b_i to b_{i-1} , reflecting
589 at b_i and refracting back to the receiver’s position. In case of parallel boundaries and isotropic conditions,
590 the real travel time T_{ij} is defined as

$$T_{ij} = \sqrt{T_{0_i}^2 + \left(\frac{X_j}{V_{rms_i}}\right)^2} + \epsilon_{ij} \quad (\text{A-1})$$

591 where ϵ_{ij} counts for the modelling error due to propagating approximations and isotropic assumptions.

592 Now, the recorded travel time $T^{(r)}$ is a combination of the real travel time T_{ij} plus a set of recording
593 errors e_{ij} , resulting in the equation

$$T_{ij}^{(r)} = \sqrt{T_{0_i}^2 + \left(\frac{X_j}{V_{rms_i}}\right)^2} + \epsilon_{ij} + e_{ij} \quad (\text{A-2})$$

594 A generalization of equations (A-1) and (A-2), uses Gaussian Process techniques, works in function
595 space instead of weight space and compensates for the lack of flexibility of the standard regression methods
596 [Rasmussen & Williams, 2006].

597 For 1D case, we assume that a set of travel times, related to a certain interface in a CMP gather, is
598 a sample of a continuous function with a hyperbolic trend. If a finite set of times in that curve follows
599 a multivariate Gaussian distribution, we can think that every reflection hyperbola in a CMP gather is a
600 Gaussian Process (GP) over offset x .

601 In a function form, the recorded travel – time curve, for a particular layer, $\mathcal{T}_i^{(r)}$ is a Gaussian Process

$$\mathcal{T}_i^{(r)}(x) | \Delta T_{0(1,\dots,i)}, \Delta V_{rms(1,\dots,i)} \sim \mathcal{GP}(m_{t_i}(x), k_i(x, x')) \quad (\text{A-3})$$

602 with mean and square exponential covariance functions

$$\begin{aligned} m_{t_i}(x) &= (t_{0_i}^2 + x^2 v_{rms_i}^{-2})^{1/2} \\ k_i(x, x') &= \sigma_{n_i} + \sigma_{s_i} \exp\left(-\frac{(x - x')^2}{d_i}\right) \end{aligned} \quad (\text{A-4})$$

603 where x and x' define two random points from the offset space in a single CMP, σ_{s_i} is a scale parameter,
604 σ_{n_i} is a noise parameter and d_i is a length parameter. The last parameters are regarded as constants or
605 can be set manually. The joint prior for both $\Delta T_{0(1,\dots,i)}$ and $\Delta V_{rms(1,\dots,i)}$ is given by

$$\begin{pmatrix} \Delta T_{0(1,\dots,i)} \\ \Delta V_{rms(1,\dots,i)} \end{pmatrix} \sim \mathcal{N}\left(\begin{pmatrix} \mu_{t_{0_i}} \\ \mu_{v_{(i)}} \end{pmatrix}, \Sigma_{(t_0, v_{rms_i})}\right) \quad (\text{A-5})$$

606 and their prior distribution is written as

$$\pi(v_{rms}, t_0) = \prod_{i=1}^n \pi(\Delta t_{0_i}, \Delta v_{rms_i}) \quad (\text{A-6})$$

607 with $\pi(\Delta t_{0_i}, \Delta v_{rms_i})$, the density of the joint prior in (A-5).

608 In a similar manner, we can express the likelihood function of the GP in (A-3) as

$$\pi(t_i^{(r)}(x) | v_{rms_i}, t_{0_i}) = \pi\left(t_i^{(r)}(x) | \Delta t_{0(1,\dots,i)}, \Delta v_{rms(1,\dots,i)}\right) \quad (\text{A-7})$$

609 Finally, the posterior distribution is given as the combination of the prior distribution (A-6) and the
610 likelihood (A-7), resulting in the following expression

$$\pi(v_{rms}, t_0 | t^{(r)}) = \pi(v_{rms}, t_0) \int_x \frac{\pi\left(t_i^{(r)}(x) | \Delta t_{0(1,\dots,i)}, \Delta v_{rms(1,\dots,i)}\right)}{\pi(t^{(r)}(x))} dx \quad (\text{A-8})$$

611 with $\pi(t^{(r)}(x))$, a normalizing constant that can be evaluated numerically.

612 A.2 2D emulator

613 For the 2D case, we expand the 1D Gaussian Process into a multi-gather representation by assuming that
 614 the variables ΔT_{0_i} , ΔV_{rms_i} , $V_{int.i}$ and ΔZ_i , for every geophysical boundary, follow a GP over the CMP
 615 positions (x_c) along a profile. As a result, for the recorded travel time $\mathcal{T}_i^{(r)}$ we have

$$\mathcal{T}_i^{(r)}(x, x_c) | \Delta T_{0_{(1, \dots, i)}}(x_c), \Delta V_{rms_{(1, \dots, i)}}(x_c) \sim \mathcal{GP}(m_{t_i}(x, x_c), k_i(x, x', x_c)) \quad (\text{A-9})$$

616 with mean and square exponential covariance functions

$$\begin{aligned} m_{t_i}(x, x_c) &= (t_{0_i}(x_c)^2 + x^2 v_{rms_i}(x_c)^{-2})^{1/2} \\ k_i(x, x', x_c) &= \sigma_{n_i}(x_c) + \sigma_{s_i}(x_c) \exp\left(-\frac{(x - x')^2}{d_i(x_c)}\right) \end{aligned} \quad (\text{A-10})$$

617 In a similar manner, as ΔV_{rms_i} and ΔT_{0_i} follow a GP, they take the following form

$$\Delta V_{rms_i}(x_c) \sim \mathcal{GP}\left(m_v(x_c), \sigma_{nv_i} + \sigma_{sv_i} \exp\left(\frac{(x_c - x'_c)^2}{d_{v_i}}\right)\right) \quad (\text{A-11})$$

$$\Delta T_{0_i}(x_c) \sim \mathcal{GP}\left(m_{t_0}(x_c), \sigma_{nt_i} + \sigma_{st_i} \exp\left(\frac{(x_c - x'_c)^2}{d_{t_i}}\right)\right) \quad (\text{A-12})$$

618 with $m_v(x_c)$, $m_{t_0}(x_c)$ polynomial functions, x_c , x'_c two different CMP locations along the profile and
 619 σ_{nv_i} , σ_{sv_i} , d_{v_i} , σ_{nt_i} , σ_{st_i} , d_{t_i} noise, scale and length parameters for $\Delta V_{rms_i}(x_c)$ and $\Delta T_{0_i}(x_c)$ respectively.
 620 The multi-gather case model, compensates for lateral variations in the velocity field. Analogous ex-
 621 pressions can link the recorded travel time $\mathcal{T}_i^{(r)}(x, x_c)$ with $V_{int(i)}(x_c)$ and $\Delta Z_i(x_c)$ allowing probabilistic
 622 estimations for all variables of interest in seismic reflection processing.